Desalination and Water Treatment
www.deswater.com
doi: 10.5004/dwt.2021.27634

234 (2021) 255–266
September

Photocatalytic degradation of Direct Red 16 dye under visible light irradiation using Fe-doped TiO_2/Al_2O_3 nanocatalyst: experimental design and optimization using a central composite design

Mohammad Rahmati*, Arjomand Mehrabani-Zeinabad, Vahid Barahimi, Ahmad Moheb

Department of Chemical Engineering, Isfahan University of Technology, Isfahan 8415683111, Iran, email: M.rahmati371@gmail.com (M. Rahmati)

Received 20 November 2020; Accepted 18 July 2021

ABSTRACT

In this study, Fe-doped TiO_2/Al_2O_3 hybrid as a visible active photocatalyst was synthesized by sol–gel technique. The characteristics of nanocatalyst with optimum composite (5.20 wt.% of Fe^{3+} and 0.27 wt. ratio of Al_2O_3) were also investigated by X-ray diffraction, field emission scanning electron microscopy and diffuse reflectance spectra (DRS). The DRS spectra approved that the adsorption wavelength of Fe-doped TiO_2/Al_2O_3 is in the visible light range (470 nm). The photodegradation of Direct Red 16 dye was carried out to evaluate the photoactivity properties of the prepared samples under visible light irradiation. The influence of weight fraction of Fe^{3+} (wt.%), Al_2O_3/TiO_2 wt. ratio and contact time on Direct Red 16 photodegradation was modeled and optimized using a central composite design based on response surface methodology. As the analysis of variance results, among significant variables, the Fe^{3+}/Ti^{4+} weight percentage has a maximum effect on the response. Also, the efficiency of the photocatalytic process for the degradation of dye was enhanced after coupling Al_2O_3 with Fe-TiO_2. Maximum dye removal was achieved by about 99% under the optimum conditions of 5.2 wt.% Fe^{3+}/Ti^{4+}, wt. ratio of 0.27 Al_2O_3/TiO_2 and contact time equally of 112.6 min. Regression analysis with the R^2 value of 0.9736 showed a good agreement between the experimental results and the predicted values.

Keywords: Photocatalytic degradation; Fe-doped TiO_2/Al_2O_3 nanocatalyst; Direct Red 16; Visible light; Response surface methodology

1. Introduction

A variety of dyes have been used in various industries like textiles. A high percent of dyes are released into wastewaters [1]. Treatment of dye waste has been an essential issue in the past decade. Treatment techniques of industries dye wastes can be generally divided into two main groups of physical–chemical and biodegradable processes. Physical processes are comprised of coagulation, flocculation, and sedimentation, surface absorption, filtration, and reverse osmosis [2]. Some of the chemical methods include reduction, oxidation, and ion-exchange processes. Biological treatment can be done under both aerobic and anaerobic conditions [1–3].

All of these treatment methods have their advantages and shortcomings. Physical processes usually require post-treatment and chemical treatment done by strong oxidants such as chlorine, and ozone is good enough but not economical. Efficiencies of biological treatments are poor due to dyes' high biodegradation resistance [4,5].

Thus, the development of low-cost and effective technologies for wastewater treatment is necessary. In recent decades, a great deal of interest has been devoted to photocatalytic processes for the removal of organic and inorganic water pollutants. In general, in photocatalytic processes by UV irradiation to a semiconductor oxide such as titanium dioxide (TiO_2), the electron/hole pairs are generated.

* Corresponding author.

Through sequences of chain reactions, primarily initiated by the formation of free radicals such as hydroxyl and superoxide anion radicals, the organic water pollutants can be oxidized until its mineralization [6–12]. Semiconductors such as ZnO, SnO_2, Al_2O_3, and TiO_2 have been used for the removal of water and wastewater pollutants. TiO_2/Al_2O_3 nanocomposite has high mechanical, chemical and thermal stability and can be used for various applications [13–16].

The semiconductor of TiO_2 with its chemical, electrical and optical characteristics such as wide bandgap, transparency in the visible range, high refractive index, high dielectric constant and ease of doping with active ions have been making it a strong candidate for various applications [17–20]. Among the anatase, rutile and brookite crystalline forms of TiO_2, anatase is known as an active catalyst for photocatalytic processes as a result of smaller particle size, high surface to volume ratio, and narrow bandgap.

However, there are still problems associated with TiO_2 photocatalytic properties such as:

(i) The meager degradation rate of organic pollutants because of the shallow surface area of the catalyst;
(ii) Excitation only through ultraviolet light and is inactive under visible light irradiation due to its broad band gap;
(iii) Short distances of charge separation within the particle that results in the fast recombination rate of the e^-/h^+ pair and consequently leads to a reduction of photocatalytic process performance.

Doping and coupling can be performed on a TiO_2 catalyst to tackle these problems, simultaneously. It has been suggested that doping with metal ions reduces bandgap and also can increase the photocatalytic activity of TiO_2 due to the reaction of electrons with metal ions on the surface [21,22].

The Fe^{3+} ion was chosen as the best candidate with a bandgap of about 2.6 eV and the same size as Ti^{4+}. Ti^{4+} and Fe^{3+} ion radius are 0.068 and 0.064, respectively [23]. Therefore, Fe^{3+} cations may be placed in TiO_2 structures or occupy network positions. In other words, doping occurs within a network or substitution. Fe^{3+} cations can act as surface traps in the TiO_2 network and extend the optical reaction of TiO_2 in the visible light range. However, there is a considerable discussion on the photocatalytic activity of Fe^{3+}-doped TiO_2. A group of researchers reported that doping with Fe^{3+} enhanced photocatalytic activity [24–27]. In some studies, it has been shown that light absorption in the photocatalytic process with Fe^{3+}-doped TiO_2 has been transmitted to the red spectrum over 650 nm [25].

Furthermore, by reduction of the recombination rate of the $e^-/h+$ pairs and consequently enhancing the corresponding photocatalytic activity, the coupling of TiO_2 with metal oxide can be performed. Alumina is a hard metal oxide with high strength and good toughness. TiO_2-Al_2O_3 nanomaterials have several interesting properties, including wear and corrosion resistance due to their thermal, chemical and mechanical stability [13,28].

The traditional one-factor-at-a-time (OFAT) approach, as the most common method for optimization, is time-consuming and expensive [29]. Moreover, this univariate approach does not show the interactions between the independent variables [30]. Therefore, currently, an effort is being made to replace this inefficient practice with effective chemometric methods [29]. The response surface methodology (RSM), as an efficient technique, has been successfully applied to various processes to analyze the effectiveness of selected factors on them and to achieve optimized processes using experimental designs, including TiO_2/UV oxidation [31,32].

This research study was performed based on two main objectives. Firstly, to synthesis a photocatalyst of efficient, low cost, affordable, and visible active (Fe-doped TiO_2/Al_2O_3) based on sol–gel technique [33]. Secondly, it was to find the optimum conditions for photocatalytic degradation of Direct Red 16 dye under visible light irradiation. This was performed using RSM based on the central composite design (CCD).

2. Experimental details

2.1. Materials

In this study, titanium tetraisopropoxide and isopropanol were used for the synthesis of the nanocatalysts. $Fe(NO_3)_3{\cdot}9H_2O$ and $AlCl_3{\cdot}6H_2O$ were used as the precursors of the iron ion and alumina to modify TiO_2, respectively. During the preparation of the Fe-doped TiO_2/Al_2O_3 solution, the solution pH was adjusted by the addition of HCl and NaOH. A list of materials used in the experimental study is presented in Table 1.

2.2. Synthesis of the Fe-doped TiO_2/Al_2O_3 by sol–gel technique

For the synthesis of the nanocatalyst, a set of solutions was prepared. The first solution was resulted from solving 0.162 g of $Fe(NO_3)_3{\cdot}9H_2O$ in 5 mL isopropanol; subsequently, the mixture was stirred for 1 h. The second solution was prepared by dissolving 0.870 g of $AlCl_3{\cdot}6H_2O$ in 10 mL isopropanol, and the mixture was stirred for 12 h. For adjusting the

Table 1
List of used chemicals

Materials	Chemical formula	Purity (wt.%)	Manufactured company
Titanium tetraisopropoxide (TTIP)	$C_{12}H_{28}O_4Ti$	99.999	Merck KGaA (Darmstadt, Germany)
Isopropanol	C_3H_7OH	99.5	Sigma-Aldrich (Germany)
Iron(III) nitrate nonahydrate	$Fe(NO_3)_3{\cdot}9H_2O$	99.99	Merck KGaA (Darmstadt, Germany)
Aluminum chloride hexahydrate	$AlCl_3{\cdot}6H_2O$	99.99	Sigma-Aldrich (Germany)
Hydrochloric acid	HCl	37	Merck KGaA (Darmstadt, Germany)
Direct Red 16	$C_{26}H_{17}N_5Na_2O_8S_2$	100	Ningbo

pH between 2–3, 3 drops of HCl 37 wt.% were added to the solution. The third solution, for the synthesis of Fe-doped TiO_2 nanocatalyst, solution number of 1 was mixed with 2.5 mL titanium tetraisopropoxide (TTIP) and 35 mL isopropanol (Fig. 1a). The solution pH was kept within the range of 2–3 by HCl 37 wt.%. The prepared solution was ultrasonicated for 20 min and stirred continuously for 12 h. For the synthesis of Fe-doped TiO_2/Al_2O_3 nanocatalyst, the second solution was added to the third solution, and the prepared solution was ultrasonicated for 20 min and stirred continuously for 12 h (Fig. 1b). The nanocatalysts were placed in an oven at 60°C for 12 h and then were calcined by leaving it in a furnace at 500°C for 2 h.

2.3. Nanocatalyst characterization

The synthesized nanocatalysts were characterized by a Philips (X'Pert PRO MPD, PANalytical Company, Netherlands) X-ray diffractometer (XRD) with Ni-filtered Cu K_α radiation (wavelength 1.5406 Å) equipped with a Ni filter. The crystal phases and the main grain size in samples were calculated by the formula as described by Nagaveni et al. [21,37]. UV-Vis diffuse reflectance spectroscopy (DRS) was used to determine the bandgap energy of the nanocatalyst and to investigate the effect of type and amount of Fe^{3+} and Al_2O_3 on UV-Vis DRS (JASCO, V-670, USA). Also, the morphology of the surface structure of the synthesized nanocatalysts was investigated by field emission scanning electron microscopy (FE-SEM, Mira3 Tescan, USA) [39].

2.4. Photoreactor

The photocatalytic degradation experiments were performed in a batch glass cylindrical reactor with an inner diameter of 70 mm, a height of 100 mm, and liquid hold up to 100 mL. The reactor was equipped with a LED light source (λ > 410 nm, 12 V/30 W) and a magnetic stirrer for homogenizing the mixture during the experiment.

2.5. Procedure and analysis

The photocatalytic degradation of Direct Red 16 from an aqueous solution was investigated under the irradiation of visible light. In order to measure the photocatalytic activity, experiments were done in a batch reactor containing the 100 mL dye solution with a concentration of 25 mg L^{-1}. After the addition of 1 g L^{-1} of the nanocatalyst, the solution was stirred at a speed of 600 rpm. Initially, the coloring solution was stirred in the presence of the catalyst for 30 min without visible light to have a complete equilibrium between solution and nanocatalyst. Then, the solution was mixed for 120 min under the radiation of visible light. All of the experiments were performed at an initial pH of 6.8. For analyzing tests, 5 mL of the solution samples were centrifuged with a speed of 5,000 rpm for a period of 15 min to separate the nanocatalyst particles. A UV-Vis spectrophotometer at a wavelength of 526 nm was used for measuring the dye concentration. The test temperature was maintained constant at 25°C.

The photocatalytic degradation efficiency was calculated according to Eq. (1):

$$\text{Degradation}(\%) = \frac{C_0 - C}{C_0} \times 100 \quad (1)$$

where C_0 and C are the initial and the final concentrations of dye in the solution, respectively.

2.6. Experimental design and optimization by RSM

In this study, Design-Expert software was used to evaluate the effect of two-component loadings (Fe^{3+}/Ti^{4+} (A, wt.%), Al_2O_3/TiO_2 (B, wt. ratio)), and operational parameters (time (C, min)) on the Direct Red 16 degradation under visible light irradiation. The three parameters (A, B, C) were chosen as independent variables, and the photocatalytic degradation efficiency of Direct Red 16 was considered as the

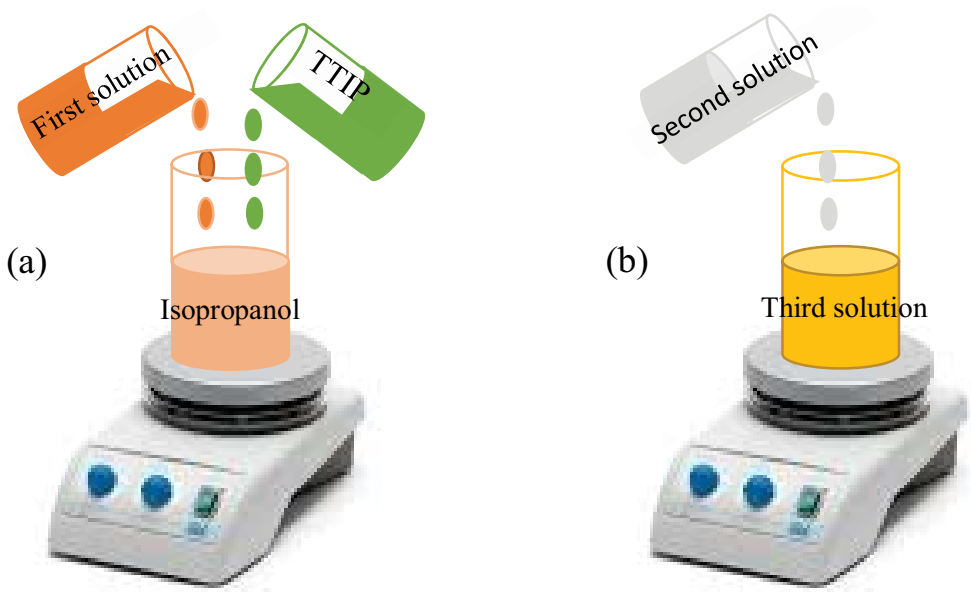

Fig. 1. Synthesis nanocatalyst (a) Fe-doped TiO_2 and (b) Fe-doped TiO_2/Al_2O_3.

dependent variable (response). The experimental ranges and the levels of the independent variables for Direct Red 16 photocatalytic degradation are shown in Table 2, and 20 experiments at these values were performed based on the arrangement specified by RSM. The effective parameters in the production of a proper Fe-doped TiO_2/Al_2O_3 nanocatalyst were investigated and optimized in the photocatalytic degradation of Direct Red 16 using the CCD at three levels.

The preliminary screening experiments were used to obtain effective Fe^{3+}/Ti^{4+} and Al_2O_3/TiO_2 concentrations values. Based on the results of these experiments that are presented in Fig. 2, the best-produced nanocatalyst for removal of the dye contained 5 and 0.2 of Fe^{3+}/Ti^{4+} and Al_2O_3/TiO_2 wt. ratio, respectively. According to the preliminary experiments, the values of 3, 5, and 7 for Fe^{3+}/Ti^{4+} wt.% and the values of 0.1, 0.2 and 0.3 for Al_2O_3/TiO_2 wt. ratio was selected for further experiments.

Moreover, a quadratic equation was obtained to relate the response variable to the three independent variables, according to Eq. (2).

$$Y = a_{00} + a_{01}A + a_{02}B + a_{03}C + a_{12}AB + a_{13}AC + a_{23}BC + a_{11}A^2 + a_{22}B^2 + a_{33}C^2 \quad (2)$$

where Y (%) is the predicted response (removal efficiency of Direct Red 16), a_{ij} are the coefficients, A, B, and C are the values of independent variables (Fe^{3+}/Ti^{4+}, Al_2O_3/TiO_2 and time, respectively). The determining conditions for photocatalytic degradation of the dye using Fe-doped TiO_2/Al_2O_3 nanocatalyst (pH = 6.8, [Fe-TiO_2/Al_2O_3] = 0.5 g L^{-1}, C_0 = 25 mg L^{-1}) by the CCD method along with the predicted and experimental values of the response are presented in Table 3. Data were analyzed by the analysis of variance (ANOVA), and the optimal values of the variables were obtained using Design-Expert software.

Table 2
Ranges and values of the variables for experimental design

Factor	Name	Levels		
		Minimum	Maximum	Mean
A	Fe^{3+}/Ti^{4+}, wt.%	3	7	5
B	Al_2O_3/TiO_2, wt. ratio	0.1	0.3	0.2
C	Time, min	40	120	80

3. Results and discussion

3.1. Characterization of TiO_2, Fe-TiO_2, Fe-TiO_2/Al_2O_3 nanocatalysts

3.1.1. X-ray diffraction analysis

X-ray diffraction (XRD) patterns of TiO_2, Fe-doped TiO_2 and Fe-doped TiO_2/Al_2O_3 samples are shown in Fig. 3. The characteristic peaks can be well indexed to the anatase phase of TiO_2. The diffraction peaks of Fe-doped TiO_2 were found to be identical to the pure TiO_2. This indicates the presence of a complete anatase phase without the crystalline phase containing iron. This could be for two reasons: (i) the low amount of doped iron ion, and (ii) the low calcination temperature applied in the preparation of the nanocatalyst that prevents the reaction of Fe^{3+} cations with TiO_2 to form new crystalline phases such as Fe_2TiO_5 and α-Fe_2O_3. Based on performed research done by Hung et al. [26], Fe_2O_3 and Fe_2TiO_5 could be formed at high calcination temperatures 600°C and 800°C, respectively [34]. The formed Fe_2TiO_5 results in the reduction of photocatalytic activity. Also, Since the ionic radius of Ti^{4+} and Fe^{3+} are almost the same, it can be inferred that Fe ions might insert into the structure of titanium and locate at interstices or occupy some of the lattice sites of TiO_2 [27], thus cause doping of iron ion to titanium.

Also, the XRD results obtained from Fe-doped TiO_2/Al_2O_3 showed that the peak position of the nanocomposite was nearly the same as the pure TiO_2 and Fe-TiO_2, thereby

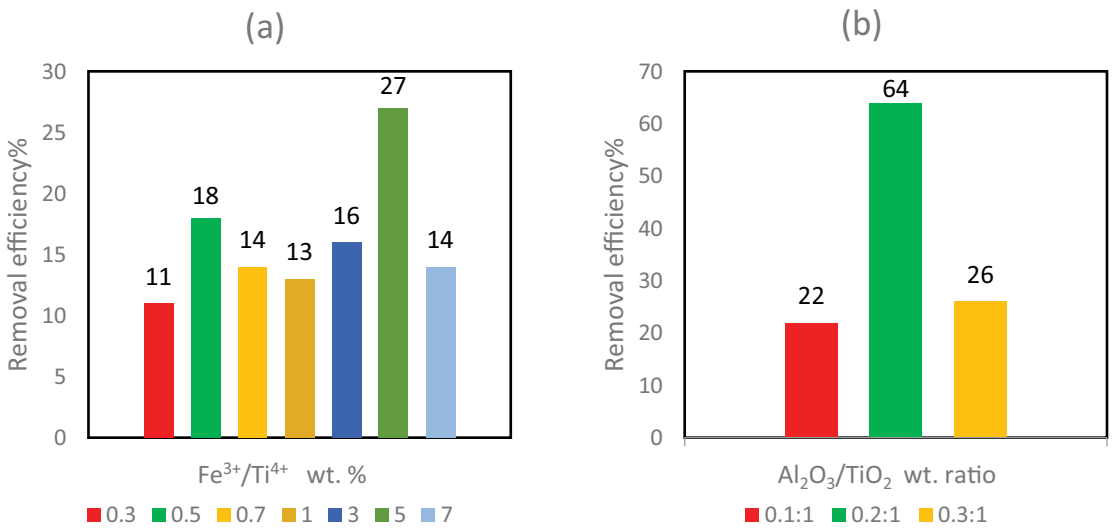

Fig. 2. Removal efficiency of the photocatalytic degradation reaction: (a) for various wt.% of Fe^{3+}/Ti^{4+}, (pH = 6.8; [Fe-TiO_2] = 0.5 g L^{-1}; C_0 = 25 mg L^{-1}; contact time = 120 min) and (b) for various wt. ratio of Al_2O_3/TiO_2, (pH = 6.8; [Al_2O_3/TiO_2] = 0.5 g L^{-1}; C_0 = 25 mg L^{-1}; contact time = 120 min).

Table 3
CCD independent variables, experimental results and predictive values

Run	Variables			Removal efficiency (%)	
	Fe^{3+}/Ti^{4+} (wt.%)	Al_2O_3:TiO_2 (wt. ratio)	Time (min)	Experimental	Predicted
1	5	0.2	80	60.0	57.5
2	5	0.1	80	44.1	38.8
3	7	0.1	40	48.0	45.0
4	5	0.2	80	57.0	57.0
5	5	0.3	80	80.4	84.0
6	5	0.2	120	79.0	79.0
7	7	0.3	40	33.5	33.5
8	5	0.2	80	64.0	57.5
9	7	0.3	120	98.0	83.9
10	3	0.3	120	90.0	77.9
11	5	0.2	80	61.4	57.0
12	3	0.1	40	7.0	6.3
13	3	0.1	120	10.0	10.9
14	5	0.2	80	61.0	57.4
15	3	0.3	40	49.0	49.0
16	7	0.2	80	56.0	62.1
17	5	0.2	40	35.0	38.8
18	7	0.1	120	95.3	100.0
19	3	0.2	80	23.0	23.0
20	5	0.2	80	45.0	57.0

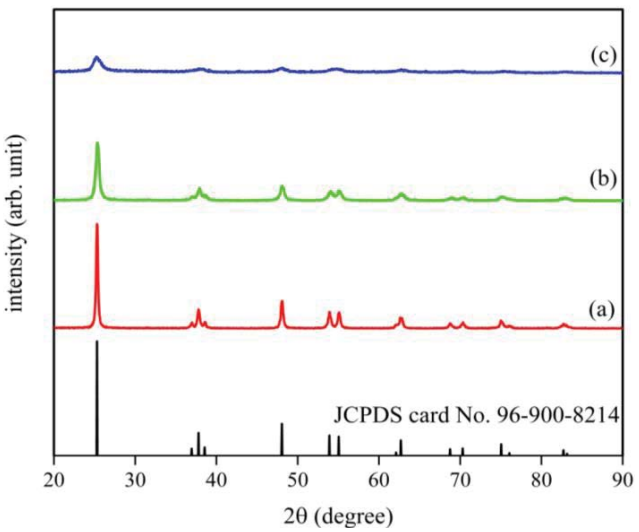

Fig. 3. XRD patterns of the samples: (a) pure TiO_2, (b) 5.2 wt.% Fe-TiO_2, and (c) 5.2 wt.% Fe-TiO_2/Al_2O_3 with wt. ratio of 0.27:1 for Al_2O_3/TiO_2.

implying all are contained in the crystallized anatase phase. However, compared to the pure TiO_2 and Fe-TiO_2, the peaks for Fe-doped TiO_2/Al_2O_3 were significantly broadened. One probable reason for this can be the smaller portion of TiO_2 in Fe-doped TiO_2/Al_2O_3 and regarding that crystalline phase in this composite is based on TiO_2, it seems logical to decrease the intensity of peaks by decreasing TiO_2 amounts in the composite. On the other hand, the duration and temperature of calcination were not enough to produce a new crystalline phase from precursors and Al_2O_3 presented in the amorphous phase. The average crystallite sizes of the samples were estimated using Scherrer's equation [30]. For the pure TiO_2, it was about 57.12 nm, it was around 40.85 nm for the 5.2 wt.% Fe-TiO_2, and it was approximately 17.85 nm for 5.2 wt.% Fe-TiO_2/Al_2O_3 with wt. ratio of 0.27:1 for Al_2O_3/TiO_2. Based on this data, the crystallite sizes of Fe-TiO_2/Al_2O_3 and Fe-TiO_2 are smaller than TiO_2 that is due to two reasons. First, TiO_2 doped with transition metals such as Fe possesses smaller particle sizes [34] since doping Fe can suppress its crystal growth or forming crystallographic point defects due to the substitution of Ti^{4+} cations by Fe^{3+} ions [35]. The second reason is the retardation of crystallite growth after adding alumina [39].

3.1.2. UV-Vis DRS technique

UV-Vis DRS for TiO_2, Fe-doped TiO_2, and Fe-doped TiO_2/Al_2O_3 is shown in Fig. 4. The results of the bandgap calculation for Fe-TiO_2 and Fe-TiO_2/Al_2O_3 catalysts were lower than of pure TiO_2. The absorption threshold of TiO_2 was 366 nm. However, the absorption peaks were gradually shifted towards the red region, 430 and 470 nm for Fe-TiO_2 and Fe-TiO_2/Al_2O_3, respectively. The bandgap energy was 3.39, 2.88, and 2.64 eV for TiO_2, Fe-TiO_2, and Fe-TiO_2/Al_2O_3, respectively, which were estimated from the absorption edge using the following equation: E (eV) = 1240 × λ^{-1} (nm). The introduced Fe^{3+} ion into TiO_2 lattice leads to create a

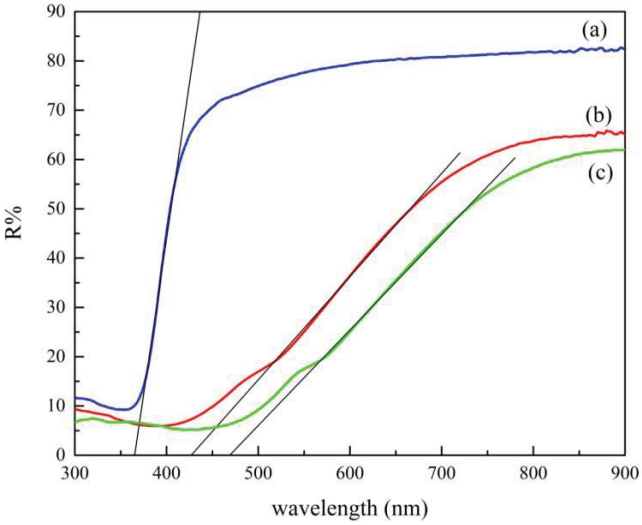

Fig. 4. UV-Vis DRS spectra: (a) pure TiO_2, (b) 5.2 wt.% Fe-TiO_2, and (c) 5.2 wt.% Fe-TiO_2/Al_2O_3 with wt. ratio of 0.27:1 for Al_2O_3:TiO_2.

new energy state between the conduction band and valence band of TiO_2 and reduce its bandgap [35].

The alumina coupling was changed the titania semiconductor from intrinsic to extrinsic. The alumina is a hole donor as the Al and Ti ions are +3 and +4 valances, respectively. So the Fermi level is moved by the presence of alumina [36].

3.1.3. FE-SEM analysis

The FE-SEM analysis was used to determine the surface morphologies of the nanocatalyst. Fig. 5 shows the images of TiO_2, Fe-doped TiO_2, and Fe-doped TiO_2/Al_2O_3 powder nanocatalyst at a scale of 200 nm. The particles measurement were performed at the points indicated in the image. These images showed that catalyst particle size is in nanoscale, and TiO_2, Fe-doped TiO_2, and Fe-doped TiO_2/Al_2O_3 are about 42, 21, and 12 nm, respectively. The FE-SEM image result is consistent with the crystallite size calculated by Scherrer's equation from the XRD data.

3.2. Model fitting and statistical analysis

3.2.1. ANOVA and response model

The obtained experimental data were analyzed, and a quadratic model is proposed. ANOVA investigated the variable impacts and their interaction in the experiment and the model significant. In this case, the quadratic model is selected, and its ANOVA analysis is shown in Table 4. The model *p*-values and *F*-values were used as a tool to check the relative significance of the variables. In general, coefficients with higher *F*-value and lower *p*-value indicate that their corresponding variables have more significance in comparison to other variables [40,41].

In this case, a *p*-value higher than 0.05 shows that the parameter is ineffective on the model and according to, Table 4 the most significant *p*-values belongs to parameters

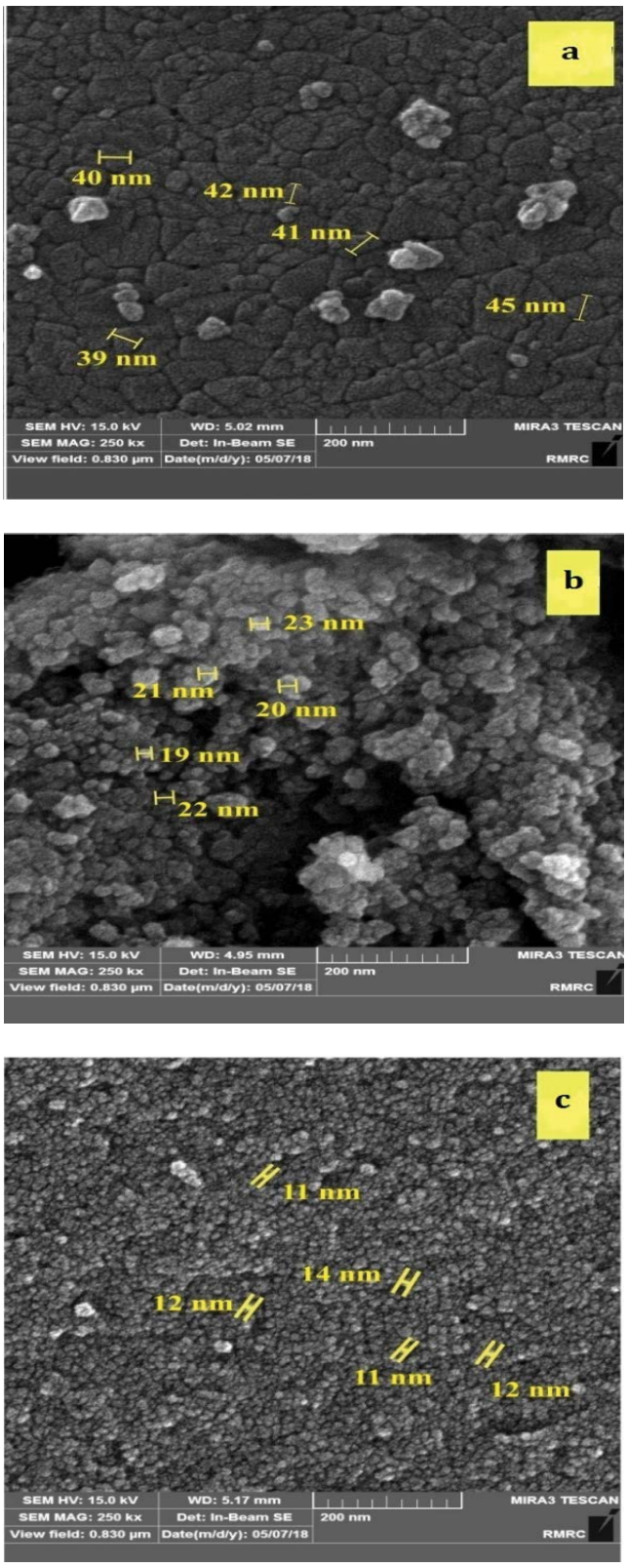

Fig. 5. FE-SEM analysis: (a) pure TiO_2, (b) 5.2 wt.% Fe-TiO_2, and (c) 5.2 wt.% Fe-TiO_2/Al_2O_3 with wt. ratio of 0.27:1 for Al_2O_3/TiO_2.

of *BC*, B^2, and C^2 with the *p*-values of 0.0963, 0.4214 and 0.8014, respectively, and eliminating these parameters

contribute to a more appropriate model. As can be seen in Table 5, all *p*-value parameters are below 0.05, which indicates the effect of these parameters in the model and using these parameters, a suitable model for data analysis is obtained. Besides the very low model *p*-value, the model *F*-value of 79.83 also showed the adequacy of the model since it was much higher than the theoretical *F*-value. Also, the lack of fit *F*-value of 1.02 indicated good predictability of the model, which implied that lack of fit was not significant relative to the pure error.

The values of R^2 and adjusted R^2 evaluates the fit of models. The R^2 value is calculated by the ratio between the variation explained by the model and the total variation of the experimental data, and its higher value is desirable [42]. Thus, the present values of R^2 (0.9736) and adjusted R^2 (0.9614) are reasonably good. Adequate precision compares the range of predicted values at the design point to the average prediction error [43]. The adequate precision of 35.083 in this study, which is well enough above 4, indicates an appropriate model.

Table 4
Power transform ANOVA results

Source	*F*-value	*p*-value	Suggestion
Model	58.08	<0.0001	Significant
A-Fe^{3+}/Ti^{4+}	132.28	<0.0001	Significant
B-Al_2O_3/TiO_2	105.93	<0.0001	Significant
C-Time	81.58	<0.0001	Significant
AB	148.30	<0.0001	Significant
AC	6.09	0.0332	Significant
BC	3.37	0.0963	Not significant
A^2	28.02	0.0004	Significant
B^2	0.70	0.4214	Not significant
C^2	0.067	0.8014	Not significant
Lack of fit	0.87	0.5590	Not significant
R-Squared	0.9655	Pred. *R*-Squared[b]	0.7704
Adj. *R*-Squared[a]	0.9345	Adeq. precision[c]	21.091

[a]Adjusted R^2; [b]Predicted R^2; [c]Adequate precision

Table 5
Power transform ANOVA results after removal of *BC*, B^2, and C^2 parameters

Source	*F*-value	*p*-value	Suggestion
Model	79.83	<0.0001	Significant
A-(Fe^{3+}/Ti^{4+})	122.16	<0.0001	Significant
B-(Al_2O_3/TiO_2)	97.83	<0.0001	Significant
C-(Time)	75.34	<0.0001	Significant
AB	136.96	<0.0001	Significant
AC	5.62	0.0338	Significant
A^2	41.06	<0.0001	Significant
Lack of fit	1.02	0.5158	Not significant
R-Squared	0.9736	Pred. *R*-Squared[b]	0.9089
Adj. *R*-Squared[a]	0.9614	Adeq. precision[c]	35.083

[a]Adjusted R^2; [b]Predicted R^2; [c]Adequate precision

From the experimental design, performed tests and gained results, an empirical second-order polynomial equation was derived to predict responses for various values of involved effective factors in the process [Eq. (3)]:

$$\left(\text{Efficiency}(\%)\right)^{0.09} = +0.53285 + 0.20141A + 2.22204B + 2.67471\text{E-}004C - 0.34123AB + 1.72867\text{E-}004AC - 0.011817A^2 \quad (3)$$

Based on the negative coefficient of A^2 resulted in a negative influence on the photocatalytic degradation of Direct Red 16. The negative coefficient of the *AB* parameter in polynomial expression indicated an antagonistic effect between these variables [30].

A comparison between experimental and predicted values of the presented model for degradation of Direct Red 16 is shown in Fig. 6. It can be seen that the high correlation between the experimental data and predicted values (R^2 = 0.9736) showed that the data fit well with the model within the studied range. On the other hand, the residuals analysis confirms the adequacy of the model. As it can be observed by the normal probability plot of the residuals (Fig. 7) and the plot of the residuals vs. the predicted response (Fig. 8). In Fig. 7, the residuals fall on a straight line suggesting the errors are distributed normally [44]. Furthermore, the structureless pattern in the plot of residuals vs. the predicted response indicated that the model is adequate, and the model does not show any violation of the independence or constant variance assumption [42].

3.2.2. Analysis of response surface

The influence of Fe^{3+}/Ti^{4+} wt.% and Al_2O_3/TiO_2 wt. ratio on the degradation efficiency while keeping contact time at 80 min is shown in Fig. 9a. As illustrated in the plots, the degradation performance increased with increasing Fe^{3+}/Ti^{4+} wt.% up to an optimal amount of about 5 wt.%. This can be based on the fact that the positively charged Fe^{3+}

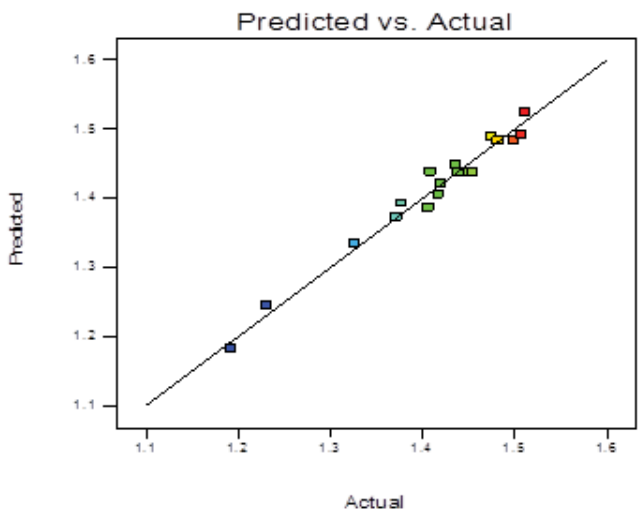

Fig. 6. Predicted vs. actual values for photocatalytic degradation of Direct Red 16.

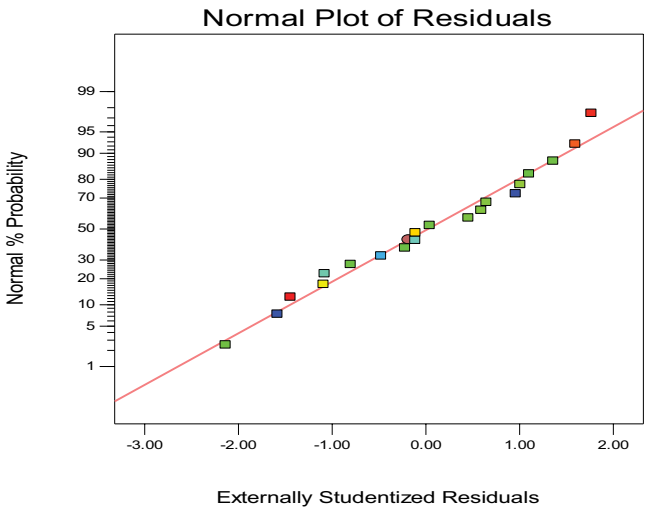

Fig. 7. Normal probability plots of the residuals.

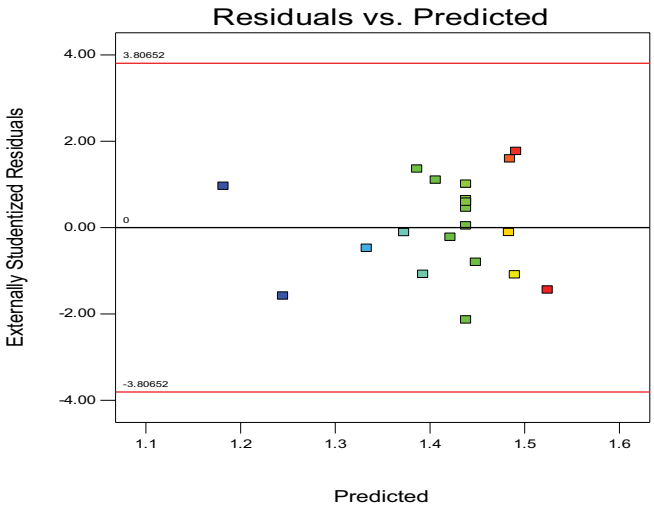

Fig. 8. The plot of the residuals against the predicted response.

adsorbed onto the TiO_2 surface is easily reduced by trapping electrons ($Fe^{3+} + e^- \rightarrow Fe^{2+}$). Reactions (4) and (5) are simultaneously performed which are desirable for the formation of $^{\bullet}OH$ and O_2^{2-} over TiO_2 surface. However, a higher amount of Fe^{3+} results in the formation of $Fe(OH)^{2+}$ ion that is a notable light-absorbing species [45]. In the part of the plots, with a reduction of Al_2O_3/TiO_2 wt. ratio, the degradation efficiency was enhanced. This could be due to the synergy between the maximum amount of doping iron ion and the minimum amount of coupling alumina.

$$Fe^{2+} + H_2O_2 + H^+ \rightarrow Fe^{3+} + {}^{\circ}OH + H_2O \quad (4)$$

$$Fe^{2+} + HO_2^{\circ} + H^+ \rightarrow Fe^{3+} + H_2O_2 \quad (5)$$

The interaction effect of Fe^{3+}/Ti^{4+} wt.% and contact time on the removal of Direct Red 16 are presented in Fig. 9b. It is evident that increasing the time increased the removal efficiency. The effect of Al_2O_3/TiO_2 wt. ratio and contact time on the removal of Direct Red 16 is shown in Fig. 9c. The reason for enhancing degradation efficiency by increasing Al_2O_3/TiO_2 wt. ratio could be due to the reduction of the rate of recombination [40], and activity enhancement.

3.2.3. Optimization of the synthesis conditions

The suggested model [Eq. (3)] was used to estimate the maximum degradation efficiency of Direct Red 16, and the corresponding parameters to achieve it. The model predicted a maximum degradation efficiency of 99% under the optimum conditions of the 5.2 wt.% Fe^{3+}/Ti^{4+}, wt. ratio of 0.27 Al_2O_3/TiO_2 and contact time equally of 112.6 min.

In order to confirm the accuracy of the proposed model, three replicate experiments were conducted under the optimum conditions. The degradation efficiency was found to be 99.0% ± 0.5%, which was reasonably close to the predicted value, and the model was successfully validated.

According to the results, the boundary of the lower bounds is considered to be the optimal final, which shows the synergistic effect of the simultaneous presence of Fe and Al_2O_3 in the TiO_2 nanocatalyst. It can be concluded that shortcoming of TiO_2 nanocatalyst can be resolved by the simultaneous application of Fe and Al_2O_3.

A comparison was made between the Fe-TiO_2/Al_2O_3 nanocatalyst and pure TiO_2 efficiencies to investigate the modified nanocatalyst. In two experiments with the same conditions (pH = 6.8, [nanocatalyst] = 0.5 g L^{-1}, C_0 = 25 mg L^{-1}), the efficiency of Fe-TiO_2/Al_2O_3 nanocatalyst was 99%, and pure TiO_2 nanocatalyst efficiency was 14% after 120 min under visible light irradiation. By comparing these two efficiencies, the effect of the modified nanocatalyst was determined in the process.

3.3. Reusability performance of Fe^{3+} (5.20 wt.%) doped-TiO_2/Al_2O_3 (0.27 wt. ratio) photocatalyst

Reusability of the Fe^{3+} (5.20 wt.%) doped-TiO_2/Al_2O_3 (0.27 wt. ratio) photocatalyst for the photodegradation of Direct Red 16 was studied at optimum conditions (pH = 6.8, [nanocatalyst] = 0.5 g L^{-1}, C_0 = 25 mg L^{-1}) after 112.6 min. Fig. 10 displays Direct Red 16 removal efficiency and recovered photocatalyst (wt.%) for 5 cycles. After the first cycle, the catalyst was recovered by centrifugation, washed with distilled water followed by illumination under visible light (1 h) to remove the adsorbed pollutants and finally dried at 100°C. The result showed that the photocatalytic activity reduces about 15% after 5 cycles. It is confirmed that the reused catalyst has a stable structure and could be used in the subsequent runs with relatively sustainable catalytic activity. The percentage of the recovered photocatalyst was about 84% after 5 cycles.

3.4. Kinetic study

The kinetic study was done to calculate the rate constant of photocatalytic degradation of Direct Red 16 for pure TiO_2, compared to optimum nanocatalysts of modified TiO_2 (Fe-TiO_2, Al_2O_3/TiO_2, and Fe-TiO_2/Al_2O_3). The pseudo-first-order kinetic model was used to study the

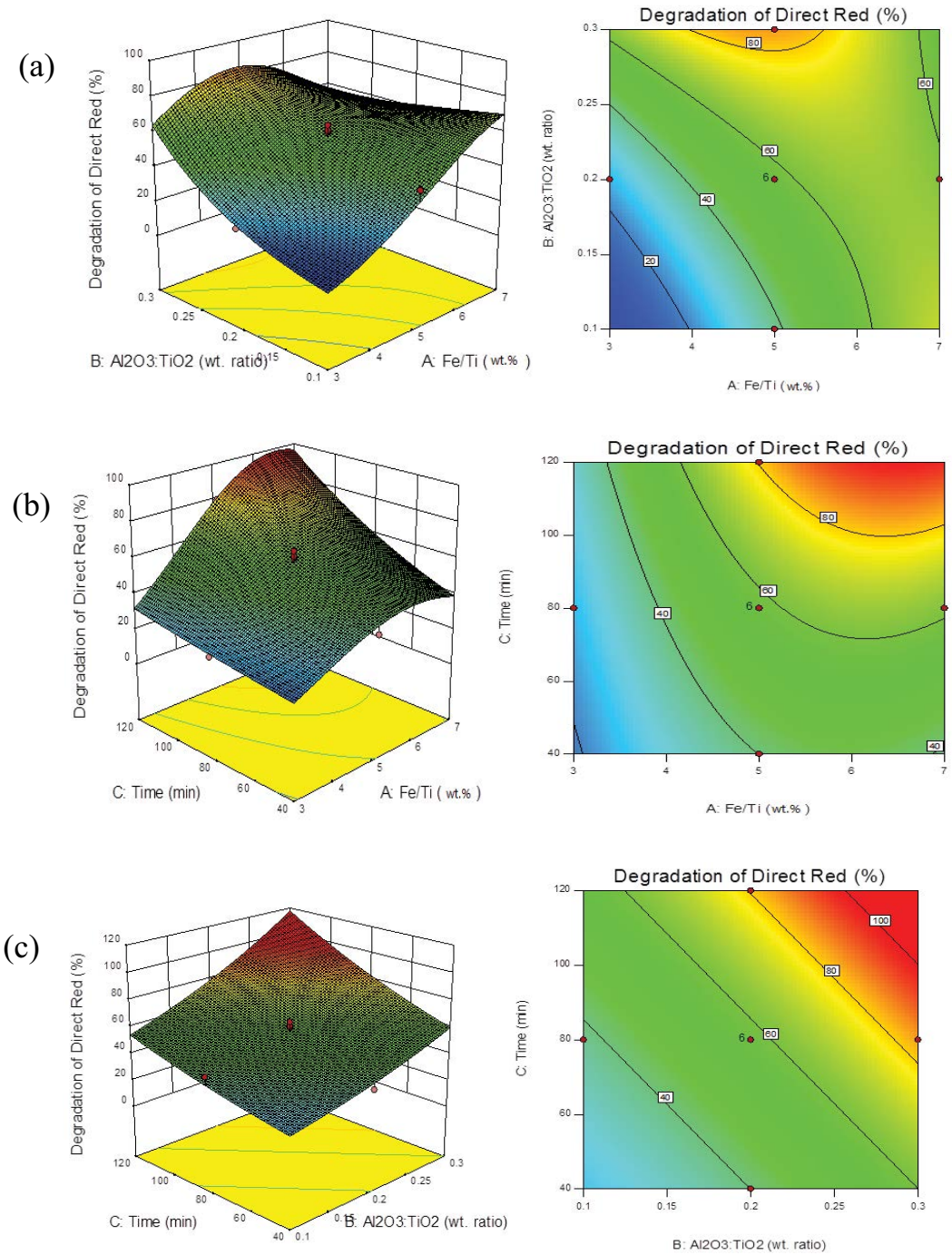

Fig. 9. Effects of Fe^{3+}/Ti^{4+} wt.%, Al_2O_3/TiO_2 wt. ratio and contact time on the degradation efficiency of Direct Red 16. (a) Contact time = 80 min, (b) Al_2O_3/TiO_2 wt. ratio = 0.2, and (c) Fe^{3+}/Ti^{4+} wt.% = 5.

photocatalytic degradation kinetic for most of the organic molecules as described:

$$-\frac{dC}{dt} = K_{ap}C \tag{6}$$

$$\ln\left(\frac{C_0}{C}\right) = K_{ap}t \tag{7}$$

where C_0, C, K_{ap}, and t are concentrations at time zero and time t, rate constant and time, respectively. The kinetic plot ($\ln(C_0/C)$ vs. irradiation time) is depicted in Fig. 11. The degradation rate constant of pure TiO_2, Fe-TiO_2, Al_2O_3/TiO_2, and Fe-TiO_2/Al_2O_3 were obtained 0.0008, 0.0027, 0.0035 and 0.0172 (min^{-1}), respectively. The Fe-TiO_2/Al_2O_3 indicates a much higher K_{ap} than pure TiO_2, Fe-TiO_2, and Al_2O_3/TiO_2, which is 21.5, 6.4, and 4.9 times respectively. It is approved more photocatalytic activity of Fe-TiO_2/Al_2O_3 nanocatalysts.

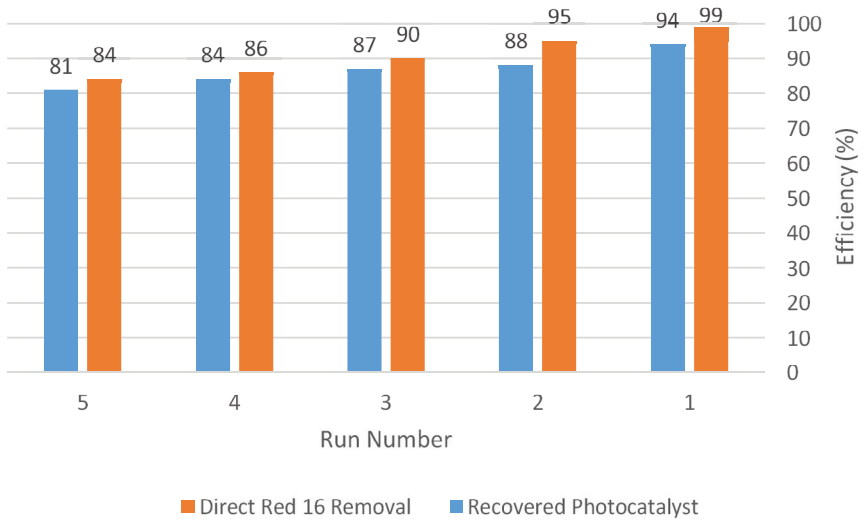

Fig. 10. Reusability results of Fe^{3+} (5.20 wt.%) doped-TiO_2/Al_2O_3 (0.27 wt. ratio) at pH of 6.8; [nanocatalyst] = 0.5 g L^{-1}; C_0 = 25 mg L^{-1}.

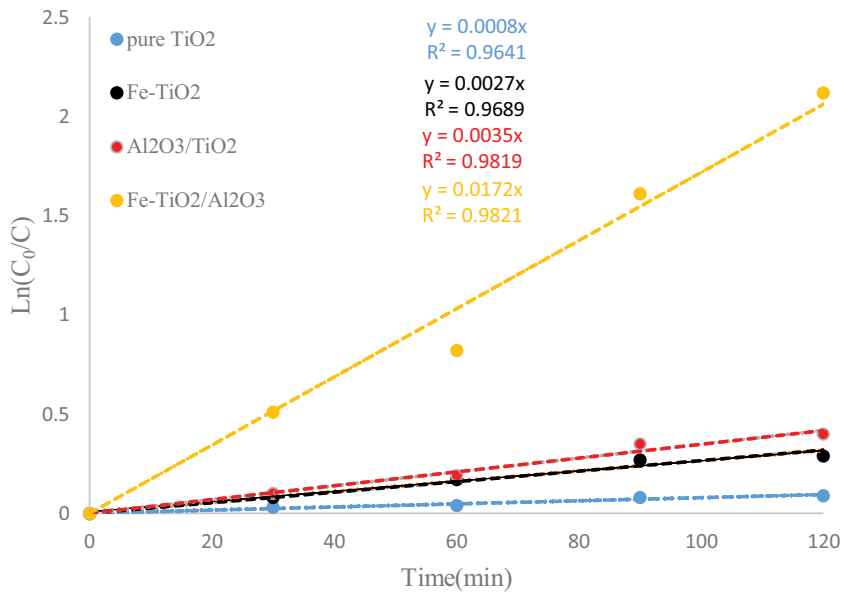

Fig. 11. The kinetic of photocatalytic degradation of Direct Red 16 (pH = 6.8; [nanocatalyst] = 0.5 g L^{-1}; C_0 = 25 mg L^{-1}).

Table 6
Summary of the results

Catalyst	Amount of sample	Pollutant	Removal percentage	Reference
Fe-TiO_2/Al_2O_3	1 g L^{-1}	Direct Red 16	99%	Present study
Fe-TiO_2/Al_2O_3	950 mg	NO_x	160% higher NO_x storage and 55% lower NO_2(g) release	[46]
TiO_2/Al_2O_3	4 g L^{-1}	Humic acid	70%	[47]
Fe-(TiO_2/Al_2O_3)	–	Methylene Blue	100%	[48]

3.5. Result comparison

The photocatalytic performance of Fe-TiO_2/Al_2O_3 or TiO_2/Al_2O_3 in dye and organic pollutant degradation was investigated by researchers. Table 6 summarizes the results of these studies.

4. Conclusions

In this study, three types of powder nanocatalysts of Fe-TiO_2, Al_2O_3/TiO_2, and Fe-TiO_2/Al_2O_3 were prepared with different ratios via sol–gel technique for photocatalytic degradation of Direct Red 16 dye. By performing the

preliminary tests, the concentrations values of Fe^{3+}/Ti^{4+} and Al_2O_3/TiO_2 were determined. Applying a quadratic model derived based on the RSM method showed that a nanocatalyst with optimum contents of 5.2 wt.% Fe^{3+}/Ti^{4+}, wt. ratio of 0.27 Al_2O_3/TiO_2 and contact time equally of 112.6 min had the best efficiency, which is consistent with the results of the performed experiment.

Based on the results, doping of TiO_2 particles by Fe^{3+}, the band-gap energy of synthesized nanocatalysts was reduced, and correspondingly the visible light activity in degradation of Direct Red 16 dye was improved. The photocatalytic activity of the synthesized nanocatalyst was enhanced by adding alumina as a support for Fe-doped TiO_2. The increasing Al_2O_3/TiO_2 wt. ratio increased the photocatalytic activity of the nanocatalysts.

References

[1] J. Abdi, M. Yahyanezhad, S. Sakhaie, M. Vossoughi, I. Alemzadeh, Synthesis of porous TiO_2/ZrO_2 photocatalyst derived from zirconium metal organic framework for degradation of organic pollutants under visible light irradiation, J. Environ. Chem. Eng., 7 (2019) 103096, doi: 10.1016/j.jece.2019.103096.

[2] V. Katheresan, J. Kansedo, S.Y. Lau, Efficiency of various recent wastewater dye removal methods: a review, J. Environ. Chem. Eng., 6 (2018) 4676–4697.

[3] I.A. Alaton, I.A. Balcioglu, Photochemical and heterogeneous photocatalytic degradation of waste vinylsulphone dyes: a case study with hydrolyzed Reactive Black 5, J. Photochem. Photobiol., A, 141 (2001) 247–254.

[4] M.A. Tariq, M. Faisal, M. Muneer, Semiconductor-mediated photocatalysed degradation of two selected azo dye derivatives, amaranth and bismarck brown in aqueous suspension, J. Hazard. Mater., 127 (2005) 172–179.

[5] E. Bizani, K. Fytianos, I. Poulios, V. Tsiridis, Photocatalytic decolorization and degradation of dye solutions and wastewaters in the presence of titanium dioxide, J. Hazard. Mater., 136 (2006) 85–94.

[6] D.F.M. Oliveira, P.S. Batista, P.S. Muller Jr., V. Velani, M.D. França, D.R. de Souza, A.E.H. Machado, Evaluating the effectiveness of photocatalysts based on titanium dioxide in the degradation of the dye Ponceau 4R, Dyes Pigm., 92 (2012) 563–572.

[7] R.J. Tayade, H. Bajaj, R.V. Jasra, Photocatalytic removal of organic contaminants from water exploiting tuned bandgap photocatalysts, Desalination, 275 (2011) 160–165.

[8] M. Mohammadi, A. Maleki, S. Zandi, E. Mohammadi, E. Ghahremani, J.K. Yang, S.M. Lee, Photocatalytic decomposition of aqueous diazinon using reduced graphene/ZnO nanocomposite doped with manganese, Desal. Water Treat., 184 (2020) 315–325.

[9] B.H. Fard, R.R. Khojasteh, P. Gharbani, Photocatalytic degradation of Direct Red 16 dye using $Ag/Ag_3VO_4/AgVO_3/GO$ nanocomposite, S. Afr. J. Chem., 73 (2020) 1–8.

[10] A. Garmroudi, M. Kheirollahi, S.A. Mousavi, M. Fattahi, E.H. Mahvelati, Effects of graphene oxide/TiO_2 nanocomposite, graphene oxide nanosheets and Cedr extraction solution on IFT reduction and ultimate oil recovery from a carbonate rock, Petroleum, (2020), doi: 10.1016/j.petlm.2020.10.002 (in Press).

[11] M. Vaez, A. Zarringhalam Moghaddam, S. Alijani, Optimization and modeling of photocatalytic degradation of azo dye using a response surface methodology (RSM) based on the central composite design with immobilized titania nanoparticles, Ind. Eng. Chem. Res., 51 (2012) 4199–4207.

[12] A. Payan, M. Fattahi, B. Roozbehani, S. Jorfi, Enhancing photocatalytic activity of nitrogen doped TiO_2 for degradation of 4-chlorophenol under solar light irradiation, Iran. J. Chem. Eng., 15 (2018) 3–14.

[13] Y. Wang, C. Li, W. Tian, Y. Yang, Laser surface remelting of plasma sprayed nanostructured Al_2O_3–13 wt.% TiO_2 coatings on titanium alloy, Appl. Surf. Sci., 255 (2009) 8603–8610.

[14] C. Anderson, A.J. Bard, Improved photocatalytic activity and characterization of mixed TiO_2/SiO_2 and TiO_2/Al_2O_3 materials, J. Phys. Chem. B, 101 (1997) 2611–2616.

[15] N. Dejang, A. Limpichaipanit, A. Watcharapasorn, S. Wirojanupatump, P. Niranatlumpong, S. Jiansirisomboon, Fabrication and properties of plasma-sprayed Al_2O_3/ZrO_2 composite coatings, J. Therm. Spray Technol., 20 (2011) 1259–1268.

[16] L. Mo, P. Lyu, Z. Yang, J. Gong, K. Liu, J. Li, Photocatalytic degradation of bagasse pulp wastewater with La-TiO_2/Al_2O_3 as a catalyst, Desal. Water Treat, 187 (2020) 256–265.

[17] R. Mechiakh, F. Meriche, R. Kremer, R. Bensaha, B. Boudine, A. Boudrioua, TiO_2 thin films prepared by sol–gel method for waveguiding applications: correlation between the structural and optical properties, Opt. Mater., 30 (2007) 645–651.

[18] Ü.Ö.A. Arıer, F.Z. Tepehan, Controlling the particle size of nanobrookite TiO_2 thin films, J. Alloys Compd., 509 (2011) 8262–8267.

[19] X. Chen, S.S. Mao, Titanium dioxide nanomaterials: synthesis, properties, modifications, and applications, Chem. Rev., 107 (2007) 2891–2959.

[20] A.L. Linsebigler, G. Lu, J.T. Yates Jr., Photocatalysis on TiO_2 surfaces: principles, mechanisms, and selected results, Chem. Rev., 95 (1995) 735–758.

[21] K. Nagaveni, M. Hegde, G. Madras, Structure and photocatalytic activity of $Ti_{1-x}M_xO_{2\pm\delta}$ (M = W, V, Ce, Zr, Fe, and Cu) synthesized by solution combustion method, J. Phys. Chem. B, 108 (2004) 20204–20212.

[22] P. Bouras, E. Stathatos, P. Lianos, Pure versus metal-ion-doped nanocrystalline titania for photocatalysis, Appl. Catal., B, 73 (2007) 51–59.

[23] M.C. Wang, H.J. Lin, T.S. Yang, Characteristics and optical properties of iron ion (Fe^{3+})-doped titanium oxide thin films prepared by a sol–gel spin coating, J. Alloys Compd., 473 (2009) 394–400.

[24] C.Y. Wang, C. Böttcher, D.W. Bahnemann, J.K. Dohrmann, A comparative study of nanometer sized Fe(III)-doped TiO_2 photocatalysts: synthesis, characterization and activity, J. Mater. Chem., 13 (2003) 2322–2329.

[25] J. Zhu, F. Chen, J. Zhang, H. Chen, M. Anpo, Fe^{3+}-TiO_2 photocatalysts prepared by combining sol–gel method with hydrothermal treatment and their characterization, J. Photochem. Photobiol., A, 180 (2006) 196–204.

[26] W.C. Hung, Y.C. Chen, H. Chu, T.K. Tseng, Synthesis and characterization of TiO_2 and Fe/TiO_2 nanoparticles and their performance for photocatalytic degradation of 1,2-dichloroethane, Appl. Surf. Sci., 255 (2008) 2205–2213.

[27] M.A. Khan, S.I. Woo, O.B. Yang, Hydrothermally stabilized Fe(III) doped titania active under visible light for water splitting reaction, Int. J. Hydrogen Energy, 33 (2008) 5345–5351.

[28] N. Dejang, A. Watcharapasorn, S. Wirojupatump, P. Niranatlumpong, S. Jiansirisomboon, Fabrication and properties of plasma-sprayed Al_2O_3/TiO_2 composite coatings: a role of nano-sized TiO_2 addition, Surf. Coat. Technol., 204 (2010) 1651–1657.

[29] V.A. Sakkas, M.A. Islam, C. Stalikas, T.A. Albanis, Photocatalytic degradation using design of experiments: a review and example of the Congo red degradation, J. Hazard. Mater., 175 (2010) 33–44.

[30] M.N. Chong, B. Jin, C.W. Chow, C.P. Saint, A new approach to optimise an annular slurry photoreactor system for the degradation of Congo Red: statistical analysis and modelling, Chem. Eng. J., 152 (2009) 158–166.

[31] D. Vildozo, C. Ferronato, M. Sleiman, J.M. Chovelon, Photocatalytic treatment of indoor air: optimization of 2-propanol removal using a response surface methodology (RSM), Appl. Catal., B, 94 (2010) 303–310.

[32] A. Khataee, M. Fathinia, S. Aber, M. Zarei, Optimization of photocatalytic treatment of dye solution on supported TiO_2 nanoparticles by central composite design: intermediates identification, J. Hazard. Mater., 181 (2010) 886–897.

[33] D. Tekin, T. Tekin, H. Kiziltaş, Synthesis and characterization of TiO_2 and Ag/TiO_2 thin-film photocatalysts and their efficiency

in the photocatalytic degradation kinetics of Orange G dyestuff, Desal. Water Treat., 198 (2020) 376–385.

[34] T. Sun, J. Fan, E. Liu, L. Liu, Y. Wang, H. Dai, Fe and Ni co-doped TiO_2 nanoparticles prepared by alcohol-thermal method: application in hydrogen evolution by water splitting under visible light irradiation, Powder Technol., 228 (2012) 210–218.

[35] Y. Yalçın, M. Kılıç, Z. Çınar, Fe^{+3}-doped TiO_2: a combined experimental and computational approach to the evaluation of visible light activity, Appl. Catal., B, 99 (2010) 469–477.

[36] E. Barajas-Ledesma, M.L. García-Benjume, I. Espitia-Cabrera, M. Ortiz-Gutiérrez, F.J. Espinoza-Beltrán, J. Mostaghimi, M.E. Contreras-García, Determination of the band gap of TiO_2–Al_2O_3 films as a function of processing parameters, Mater. Sci. Eng., B, 174 (2010) 71–73.

[37] P.N. Panahi, S. Babaei, M.H. Rasoulifard, Synthesis and visible-light photocatalytic activity of nanoperovskites and exploration of silver decoration to enhance photocatalytic efficiency, Desal. Water Treat., 194 (2020) 194–202.

[38] M. Hu, X. Wang, H. Liu, N. Li, T. Li, R. Zhang, D. Chen, Visible-light-driven photodegradation of aqueous organic pollutants by $Ag/AgCl@Zn_3V_2O_8$ nanocomposites, Desal. Water Treat., 86 (2017) 102–114.

[39] J.Y. Kim, S.H. Kang, H.S. Kim, Y.E. Sung, Preparation of highly ordered mesoporous Al_2O_3/TiO_2 and its application in dye-sensitized solar cells, Langmuir, 26 (2009) 2864–2870.

[40] V. Barahimi, H. Moghimi, R.A. Taheri, Cu doped TiO_2-Bi_2O_3 nanocomposite for degradation of azo dye in aqueous solution: process modeling and optimization using central composite design, J. Environ. Chem. Eng., 7 (2019) 103078, doi: 10.1016/j.jece.2019.103078.

[41] E.L. Pereira, A.C. Borges, F.F. Heleno, K.R. de Oliveira, G.J. da Silva, A.H. Mounteer, Central composite rotatable design for startup optimization of anaerobic sequencing batch reactor treating biodiesel production wastewater, J. Environ. Chem. Eng., 7 (2019) 103038, doi: 10.1016/j.jece.2019.103038.

[42] M.Y. Noordin, V.C. Venkatesh, S. Sharif, S. Elting, A. Abdullah, Application of response surface methodology in describing the performance of coated carbide tools when turning AISI 1045 steel, J. Mater. Process. Technol., 145 (2004) 46–58.

[43] R.D.C. Soltani, A. Rezaee, H. Godini, A.R. Khataee, A. Hasanbeiki, Photoelectrochemical treatment of ammonium using seawater as a natural supporting electrolyte, Chem. Ecol., 29 (2013) 72–85.

[44] B.K. Körbahti, M.A. Rauf, Determination of optimum operating conditions of carmine decoloration by UV/H_2O_2 using response surface methodology, J. Hazard. Mater., 161 (2009) 281–286.

[45] L. Wei, C. Shifu, Z. Wei, Z. Sujuan, Titanium dioxide mediated photocatalytic degradation of methamidophos in aqueous phase, J. Hazard. Mater., 164 (2009) 54–160.

[46] A.M. Soylu, M. Polat, D.A. Erdogan, Z. Say, C. Yıldırım, O. Birer, E. Ozensoy, TiO_2–Al_2O_3 binary mixed oxide surfaces for photocatalytic NO_x abatement, Appl. Surf. Sci., 318 (2014) 142–149.

[47] S. Xu, X. Zhang, J. Ng, D.D. Sun, Preparation and application of TiO_2/Al_2O_3 microspherical photocatalyst for water treatment, Water Sci. Technol. Water Supply, 9 (2009) 39–44.

[48] A.H. Haghighaty, S.M. Dehaghi, Resistant in alkaline media core-shell photocatalyst of $Fe(TiO_2/Al_2O_3)$ for degradation of water pollutant, Orient. J. Chem., 34 (2018) 1046, doi : 10.13005/ojc/340256.